Computational hemodynamic indices to identify Transcatheter Aortic Valve Implantation degeneration

Luca Crugnola [a,*], Christian Vergara [a], Laura Fusini [b,c], Ivan Fumagalli [d], Giulia Luraghi [a], Alberto Redaelli [c], Gianluca Pontone [b,e]

[a] LaBS, Department of Chemistry, Materials and Chemical Engineering "Giulio Natta", Politecnico di Milano, Piazza Leonardo da Vinci 32, Milan, 20133, Italy
[b] Department of Perioperative Cardiology and Cardiovascular Imaging, Centro Cardiologico Monzino IRCSS, via Carlo Parea 4, Milan, 20138, Italy
[c] Department of Electronics, Information and Bioengineering, Politecnico di Milano, Via Giuseppe Ponzio 34, Milan, 20133, Italy
[d] MOX, Department of Mathematics, Politecnico di Milano, Via Edoardo Bonardi 9, Milan, 20133, Italy
[e] Department of Biomedical, Surgical and Dental Sciences, Università degli studi di Milano, Via della Commenda 10, Milan, 20122, Italy

ARTICLE INFO

ABSTRACT

Background and Objectives: Structural Valve Deterioration (SVD) is the main limiting factor to the long-term durability of the bioprosthetic valves used for Transcatheter Aortic Valve Implantation (TAVI), a minimally invasive technique for the treatment of severe aortic stenosis. The aim of this retrospective study is to perform patient-specific computational analyses of blood dynamics shortly after TAVI to identify hemodynamic indices that correlate with a premature onset of SVD which is detected at 5-10 years long-term follow-up exam after TAVI.

Methods: The study population comprises fourteen patients: seven cases with SVD at long-term follow-up were identified and seven cases without SVD were randomly extracted from the same cohort. Starting from pre-operative CT images, we created trustworthy post-TAVI scenarios by virtually inserting the bioprosthetic valve (stent and leaflets) and we qualitatively validated such virtual scenarios against post-TAVI CT scans, when available. We then performed numerical simulations imposing personalized inlet conditions based on patient-specific Echo Doppler cardiac output measurements and the numerical results were post-processed to identify suitable hemodynamics indices with the aim of discriminating between the SVD and non-SVD groups of patients. In particular, differences in terms of each individual index were evaluated using a Wilcoxon rank-sum test. Moreover, we defined three synthetic scores, based on suitably scaled hemodynamic indices of stress and vorticity, evaluated in different contexts: on the leaflets, in the ascending aorta, and in the whole domain.

Results: We found that the hemodynamic index related to leaflets' OSI individually shows statistically significant differences (p=0.007) between the SVD and non-SVD groups. Moreover, our proposed synthetic scores are able to clearly isolate the SVD group both in a two-dimensional space given by the aorta and leaflets scores and by only considering the global synthetic score.

Conclusion: The results of this computational study suggest that blood dynamics may play an important role in creating the conditions that lead to SVD. Moreover, the proposed synthetic scores could provide further indications for clinicians in assessing and predicting TAVI valves' long-term performance.

1. Introduction

Transcatheter Aortic Valve Implantation (TAVI) is a minimally invasive technique for the treatment of severe Aortic Stenosis (AS). It consists in the deployment of a stented bioprosthetic valve inside the native aortic valve via a percutaneous catheter, restoring a physiological function of the aortic orifice. Introduced in 2002 as an alternative to open-heart Surgical Aortic Valve Replacement, TAVI has become the standard of care for patients with severe AS at prohibitive surgical risk, and the preferred treatment for many intermediate and high-risk elderly patients [1,2]. Moreover, the results of the recent PARTNER 3 and Evolut Risk clinical trials suggest that TAVI might be the preferred option for AS treatment even in low-risk younger patients [3–6].

Assessing the long-term durability of TAVI valves is of utmost importance in order to extend the TAVI procedure to younger patients with longer life expectancy. However, TAVI is a fairly new technique, thus there is a lack of long-term follow-up data; moreover, available

data are mostly related to older generation devices implanted on elderly patients, having limited life expectancy [7]. Therefore, the prediction of TAVI effectiveness and the understanding of the mechanisms underlying degeneration over the years are nowadays still challenging issues.

Structural Valve Deterioration (SVD) leading to regurgitation or stenosis is the main limiting factor to the long-term durability of TAVI bioprosthetic valves [8,9]. This is an irreversible process manifested by gradual degenerative changes in the bioprosthesis, such as pannus growth, leaflet fibrosis and calcification, possibly leading to ruptures and perforations of the leaflets [10]. Recent studies provided evidence that multiple processes are involved in SVD pathogenesis, including immune rejection and atherosclerosis-like tissue remodeling [9,10], suggesting a possible influence of aortic hemodynamics on the development of SVD [11].

Computational models have been extensively employed within the TAVI framework. A structural analysis, via the Finite Element Method, has been usually applied to study the implantation of the bioprosthetic valve, assessing the impact of device design and anatomical features on the outcome of the intervention [12–14]. Post-TAVI hemodynamics have been numerically simulated using Computational Fluid Dynamics (CFD) or Fluid-Structure Interaction approaches, usually investigating complications such as para-valvular leakage, embolism risk, and thrombogenicity [15–17]. The investigation in [11] represents the first computational hemodynamic study focusing on SVD, where a few patient-specific cases were analyzed to explore possible relations between hemodynamics shortly after the TAVI procedure and the long-term degeneration of the bioprosthetic valves. In particular, the authors correlated the early post-TAVI stress distribution on the proximal aortic wall with the presence of SVD detected at 5–10 years follow-up exams.

In the current work, we delve deeper into this analysis, overcoming the main limitations of [11], which are: (i) the focus on the sole systolic phase; (ii) the reduced number of patients analyzed; (iii) the absence in the geometric model of the bioprosthetic valve's leaflets; (iv) the use of the same boundary conditions for each patient. This allows us to propose effective hemodynamic indices in early post-TAVI stages that correlate with the premature onset of SVD, detected at 5–10 years follow-up exam after TAVI. In particular, the main objectives and advancements with respect to [11] can be summarized as follows:

- A complete computational-hemodynamics investigation of fourteen patients, comprising the whole heartbeat (systole and diastole), the presence of the bioprosthetic valve's leaflets, and a turbulence model;
- The prescription of a realistic inlet flow rate condition tuned on patient-specific post-operative cardiac output measurements;
- The definition of new hemodynamic-based synthetic scores, obtained by combining different indices that are easily computable as post-processing of the numerical simulations, able to discriminate between patients with and without SVD at follow-up exam.

To this aim, we start from pre-operative Computed Tomography (CT) images and we perform a virtual implantation of the bioprosthetic valve to obtain trustworthy early post-TAVI computational scenarios, representative of few days after the intervention.

The analyses of this work are strongly based on the assumption that hemodynamics in early post-TAVI stages can influence the long-term degeneration of the implanted valves. This can be motivated by the creation of specific hemodynamic conditions which trigger a cascade of events possibly contributing to deterioration [10].

2. Methods

In this work, we present a retrospective computational study aiming at finding hemodynamic indications about Structural Valve Deterioration (SVD). This encompasses the following steps:

1. Virtual implantation of a bioprosthetic valve inside patient-specific aortic root geometries, reconstructed from pre-operative CT scans;
2. Patient-specific CFD analysis of early post-TAVI hemodynamics, performed in the virtual scenarios obtained after step 1., when the bioprosthetic valve is yet to be degenerated;
3. Post-processing of the CFD results to identify hemodynamic indices that correlate with the presence of SVD detected at 5–10 years follow-up exam.

This is done with the prospective aim of employing our model in a clinical setting, in order to predict TAVI valves' degeneration and provide indications for a personalized follow-up planning. Analogously to what is done by companies such as FEops (https://www.feops.com/) and HeartFlow (https://www.heartflow.com/), we introduce in our model some simplifications in order to reduce the computational cost of the numerical simulations:

- Cylindrical shape of the virtually implanted stent is assumed; no Finite Elements deployment simulation is performed to recover the open configuration of the stent (see Section 2.2);
- The bioprosthetic leaflets dynamics is described in an on/off modality and no Fluid-Structure Interaction is accounted for (see Section 2.2);
- Rigid aortic walls are assumed (see Section 2.3).

Such simplifications will be discussed in Section 4.

In what follows we present the available clinical data (Section 2.1) and the generation of patient-specific early post-operative virtual scenarios (Section 2.2); then, we describe the mathematical and numerical models for aortic hemodynamics in presence of the TAVI bioprosthetic valve (Section 2.3), and we discuss the prescription of inlet boundary conditions (Section 2.4); finally, we introduce the analyzed hemodynamic indices and we build synthetic SVD-discriminating scores (Section 2.5).

2.1. Clinical data

Seven cases of patients who underwent TAVI between 2008 and 2012 showing SVD at 5–10 years long-term follow-up were identified and seven cases without SVD at same exam were randomly extracted from the same cohort and matched for baseline characteristics. We refer to the former group as DEG patients and to the latter one as NODEG patients. The mean follow-up time is 7.2 ± 1.9 years. The definition of SVD is in accordance with "SVD stage 3", i.e. when the implanted valve is characterized by severe stenosis and/or regurgitation, see [18] for further details. The study was approved from IRB of Centro Cardiologico Monzino and registered with number R1264/20.

In this study we consider only patients who received a first or second generation Edwards SAPIEN balloon-expandable valve with size 23 mm, which is the most likely to develop SVD between the Edwards SAPIEN valves [3]. In particular, it consists of a trileaflet valve made of bovine pericardium mounted on cobalt-chromium stent with an external diameter of 23 mm and a height of 14.5 mm. On the ventricular side of the stent frame, an inner polyethylene terephthalate fabric skirt is applied [11,19] (see Fig. 1(a)).

For each patient we have at disposal:

- a pre-operative CT scan taken at late diastole with a Discovery HD750 scanner (GE Healthcare) using the following configuration: 64×0.625 mm; gantry rotation time 350 ms; tube voltage, 120 kVp; and effective tube current, 650 mA. Contrast enhancement was achieved with a triphasic injection of an 80 ml bolus of Iomeron 400 mg/ml (Bracco Imaging S.p.A.) through an antecubital vein at a 5 ml/s infusion rate, followed by 50 ml of saline solution, and a further 50 ml bolus of contrast at 3.5 ml/s [3].
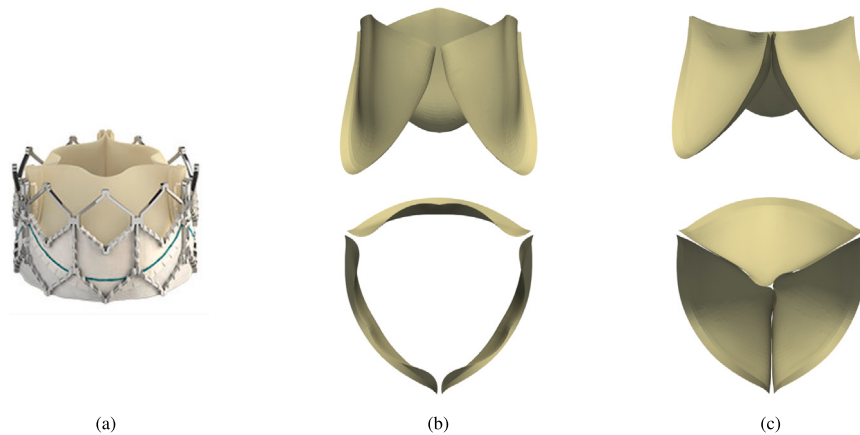
(a)   (b)   (c)

Fig. 1. (a) Edwards SAPIEN-XT bioprosthetic valve (source *Medical Expo*: https://www.medicalexpo.com/). (b)–(c) Trileaflet models obtained in [20] from a structural numerical simulation: (b) open configuration, (c) closed configuration.

- early post-TAVI Doppler Transthoracic Echocardiography (TTE) data obtained with commercially available equipment (iE33 or Epiq, Philips Medical System, or Vivid-9, GE Healthcare) [3] between two days and seven months after the implantation. Specifically, these data allow us to obtain patient-specific cardiac output measurements used to impose boundary conditions (see Section 2.4).

Moreover, we have also at disposal for some patients early post-TAVI Continuous wave Doppler TTE data, providing information on the maximum blood velocity reached through the aortic valve (see Section 3.3 for the complete list), and for patients DEG1 and NODEG1 CT scans taken some years after TAVI.

2.2. Post-operative virtual domain generation

We build post-TAVI computational domains starting from pre-operative CT scans. The procedure is carried out using the Vascular Imaging Toolkit (VMTK, http://www.vmtk.org [21]) and Paraview (https://www.paraview.org) software, and comprises the following steps:

1. Reconstruction of the aortic root geometry and calcium deposits from the pre-operative CT scan;
2. Virtual implantation of the bioprosthetic valve's stent inside the pre-operative reconstructed aortic root;
3. Positioning of suitable leaflets geometries, taken from [20], inside the virtually implanted stent;
4. Generation of the volumetric mesh.

The first two steps of the procedure are detailed in [11]. In particular, the virtual stent, modeled as a hollow cylinder, is oriented using the centerline of the reconstructed pre-operative aortic geometry and positioned at the barycenter of the aortic annulus. The virtual stent is then rigidly translated along its radial direction to account for the patient-specific calcification pattern on the native aortic valve. Finally, the reconstructed aortic annulus is possibly circularized and expanded in case of a dimensional mismatch with the bioprosthetic valve, analogously to what happens during TAVI due to the balloon inflation. The resulting computational domain is shown for one patient in Fig. 2(a) and comprises: the aortic wall downstream the aortic annulus, the interface between blood and the aortic annulus, the interface between blood and the stent, an inlet section and a outlet section.

One of the major advancements of this work with respect to [11] is the introduction of the bioprosthetic valve's leaflets (step 3 in the list above). We use a leaflets' geometry taken from another study [20] and scale it in order to fit the dimensions of the 23 mm Edwards SAPIEN valves analyzed in this work (see Section 2.1). In [20], the authors

considered an idealized trileaflet model, which mimics the native aortic valve morphology, and applied a physiological pressure gradient to obtain the open and closed configurations of the leaflets (Figs. 1(b)–1(c)). In particular, the pressure gradient, ranging from -81.07 mmHg to 1.95 mmHg, was directly applied on the aortic side of the leaflets in a structural Finite Element analysis. Notice that, the mechanical properties of the leaflets were set to represent pericardium and thus they are suited to model an Edwards SAPIEN valve whose leaflets are made of the same material.

The leaflets are positioned inside the virtually implanted stent by exploiting the centerline of the generated computational domain (see Fig. 2(b)). In particular, in accordance with common clinical practice [22], we orient the bioprosthetic leaflets in order to match the native ones, thus to match with the reconstructed sinuses of Valsalva (see Fig. 2(c)). Note that the thickness of the leaflets will be defined directly inside the mathematical model (see Section 2.3). The open and closed configurations of the leaflets are used to provide a quasi-static on/off modeling of opening/closure dynamics. Specifically, we perform a numerical experiment where at each time instant only one of the two rigid configurations acts as an obstruction to the fluid flow (see Section 2.3), in agreement with the flow rate profile imposed at the inlet (see Section 2.4), which identifies the systolic and diastolic phases.

Finally, a volumetric mesh is generated inside the computational domain (see Fig. 2(d)). For all fourteen patients, tetrahedral meshes were generated using VMTK with an average mesh size of approximately 1 mm, a local refinement of 0.25 mm close to the bioprosthetic valve's leaflets and a boundary layer composed of three layers close to the aortic wall (finest layer's thickness $= 0.14$ mm). The mesh size is chosen after a mesh convergence analysis, as shown in Section 3.1.

2.3. Mathematical and numerical methods

We are interested in studying aortic blood dynamics in presence of the TAVI bioprosthetic valve. We model blood as an incompressible homogeneous Newtonian fluid, as it is common practice in large vessels like the aorta [23], thus describing its dynamics with the Navier–Stokes equations.

Our computational domain is the one resulting from the post-operative virtual domain generation procedure described in Section 2.2 (Fig. 2(a)). In particular, the aortic wall and the interfaces between blood and both the stent and the aortic annulus are treated as rigid boundaries. A flow rate condition is imposed at the inlet boundary, whereas a physiological pressure $P_{Wig}(t)$, representing a Wiggers aortic pressure (Fig. 3(a)) profile, is imposed at the outlet boundary.

We account for the presence of turbulence inside the ascending aorta [24] by using the Large Eddy Simulation (LES) model, thus
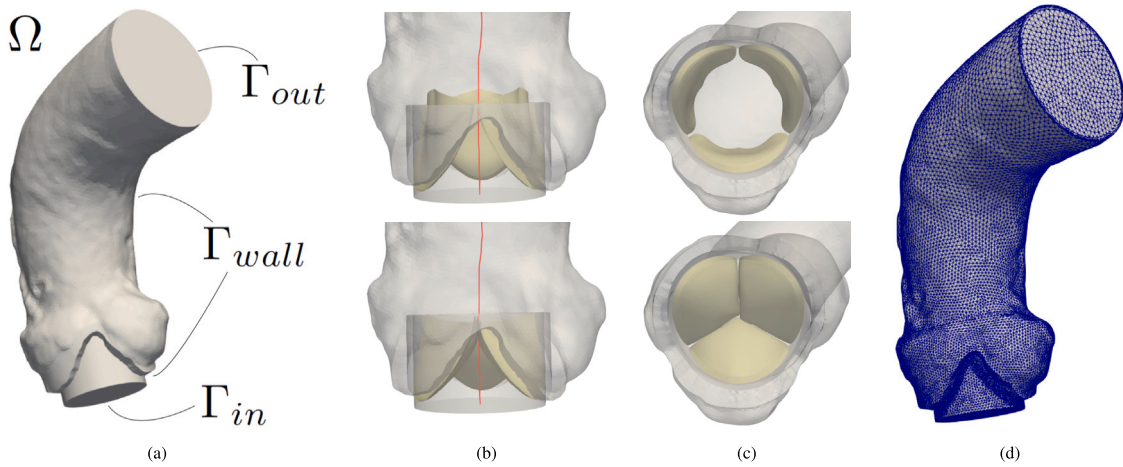
Fig. 2. (a) Computational domain Ω for one patient. Γ_{in} is the inlet boundary; Γ_{out} is the outlet boundary; Γ_{wall} is the wall, composed of the aortic wall, the interface between blood and the aortic annulus and the interface between blood and the bioprosthetic valve's stent. (b) Bioprosthetic leaflets positioned inside the virtually implanted stent using the centerline of computational domain (top: open configuration, bottom: closed configuration). (c) Orientation of the bioprosthetic leaflets in agreement with the reconstructed sinuses of Valsalva (top: open configuration, bottom: closed configuration). (d) Volumetric computational mesh with a boundary layer close to the aortic wall and a local mesh refinement close to the bioprosthetic leaflets.
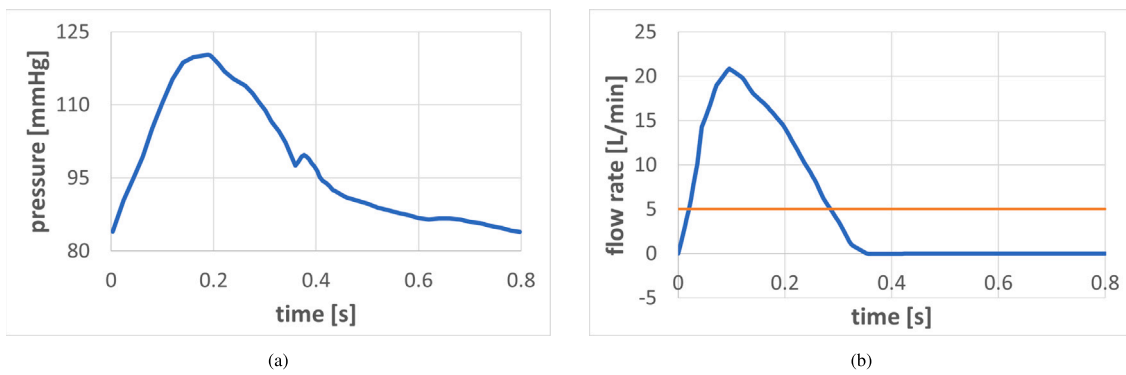
Fig. 3. (a) Wiggers aortic pressure profile imposed at outlet section. (b) Physiological flow rate waveform (mean value: 5 L/min) used to impose inlet boundary conditions. Patient-specific mean flow rate values are recovered for each patient according to the cardiac output measurements reported in Table 1.

adding a viscous term which accounts for the non-resolved scales, in particular the σ-model [25], which is suited for closed channel flows [26], specifically for hemodynamics [27,28]. The bioprosthetic valve's leaflets are implicitly represented as an obstruction to the flow using the Resistive Immersed Implicit Surface (RIIS) method [29,30], thus adding to the momentum equation of the Navier–Stokes system a local penalization term, which represents the adherence of the blood to the leaflets. In particular, a smoothed Dirac delta function is used to impose the penalization term only in a neighborhood of the immersed surface.

The resulting strong formulation of the considered mathematical model reads: given the initial blood velocity $\mathbf{u}_0$, for each time $t > 0$, find the blood velocity $\mathbf{u}$ and the blood pressure p, such that:

$$\rho\left(\frac{\partial \mathbf{u}}{\partial t} + \mathbf{u} \cdot \nabla \mathbf{u}\right) - \nabla \cdot \left[2(\mu_{sgs}(\mathbf{u}) + \mu)D(\mathbf{u})\right] + \nabla p + \delta_{\Sigma,\epsilon}\frac{R}{\epsilon}(\mathbf{u} - \mathbf{u}_{\Sigma}) = \mathbf{0} \quad \text{in } \Omega \tag{1a}$$

$$\nabla \cdot \mathbf{u} = 0 \quad \text{in } \Omega \tag{1b}$$

$$\mathbf{u} = \mathbf{0} \quad \text{on } \Gamma_{wall} \tag{1c}$$

$$p\mathbf{n} - 2(\mu_{sgs}(\mathbf{u}) + \mu)D(\mathbf{u})\mathbf{n} = P_{Wig}(t)\mathbf{n} \quad \text{on } \Gamma_{out} \tag{1d}$$

$$\int_{\Gamma_{in}} \mathbf{u} \cdot \mathbf{n} \, d\gamma = \Phi(t) \quad \text{on } \Gamma_{in} \tag{1e}$$

where $\rho = 1060$ kg/m^3 and $\mu = 3.5 \times 10^{-3}$ Pa s are the blood density and viscosity, respectively, and μ_{sgs} is the sub-grid scale viscosity introduced by the LES σ-model, which depends on the velocity field [25]; $D(\mathbf{u}) = \frac{\nabla \mathbf{u} + \nabla^T \mathbf{u}}{2}$, where the apex T stands for transpose, is the strain rate tensor; the last term of Eq. (1a) represents the RIIS method: Σ is the bioprosthetic leaflets surface, R represents a resistance coefficient, ϵ is a numerical parameter representing the half-thickness of a smoothed Dirac delta function $\delta_{\Sigma,\epsilon}$ centered in Σ and $\mathbf{u}_{\Sigma}$ is the velocity of the bioprosthetic leaflets. The value of the resistance coefficient $R = 10^5$ Kg/m s has been empirically tuned to effectively obstruct the flow close to the leaflets. Instead, notice that the smoothed delta function $\delta_{\Sigma,\epsilon}(\mathbf{x})$ gives the amount of penalization that the RIIS term introduces in the point $\mathbf{x}$; thus, points close to the delta boundary are little penalized, whereas points at the center of the delta are greatly penalized. This suggests that the effective thickness of the leaflets we are introducing to obstruct the flow is (statistically) equal to half of the delta thickness, that is ϵ. For this reason, we select $\epsilon = 0.4$ mm which is in accordance with literature values for the Edwards SAPIEN leaflets (0.36 mm) [31]. Moreover, according to the on/off modeling used in this work for the valve dynamics (see Section 2.2), we set $\mathbf{u}_{\Sigma} = \mathbf{0}$. The choice of the prescribed flow rate $\Phi(t)$ will be discussed in Section 2.4.

Being a defective condition, Eq. (1e) is not enough to guarantee existence and uniqueness of a solution. In order to prescribe such condition, we exploit an augmented weak formulation of the Navier–Stokes problem, as proposed in [32,33]. In this approach the flow rate boundary condition on Γ_{in} is considered as a constraint for the solution

Table 1

Cardiac output measurements obtained from early post-TAVI Doppler TTE data and used to adapt the waveform in Fig. 3(b) in order to impose for each patient the patient-specific mean flow rate value at the inlet section.

ID	CO [L/min]	ID	CO [L/min]
DEG1	5.90	NODEG1	5.35
DEG2	6.05	NODEG2	4.50
DEG3	5.45	NODEG3	5.45
DEG4	4.85	NODEG4	5.10
DEG5	5.45	NODEG5	4.35
DEG6	5.95	NODEG6	5.85
DEG7	5.30	NODEG7	5.05

and enforced using a Lagrange multiplier. In particular, the problem is closed by imposing that the traction on Γ_{in} is normal to the surface and constant in space. From the properties of the weak formulation used to treat the differential problem, it is possible to show that the physical meaning of the Lagrange multiplier relies precisely in the value of this scalar traction as a function of time [32]. Thus, with this strategy we are in fact prescribing a Neumann (traction) inlet condition where the prescribed value (the Lagrange multiplier) is at each time unknown and found by the augmented formulation. This allows us to impose the desired flow rate evolution at the inlet boundary without fixing a spatial profile for the velocity field, which would highly influence the results of the numerical simulations.

For the time discretization of the continuous problem we consider a first order implicit backward Euler scheme with an explicit treatment of the convective field and the sub-grid scale viscosity $\mu_{sgs}(\mathbf{u})$. We consider a time-step $\Delta t = 10^{-3}$ s chosen after performing a sensitivity analysis, analogous to the one for the mesh size (see Section 3.1). For space discretization we employ piece-wise linear finite elements for the velocity and pressure fields with a Streamline Upwind Petrov–Galerkin/Pressure Stabilizing Petrov–Galerkin (SUPG/PSPG) stabilization scheme [28,34,35]. At the outlet boundary we add a backflow stabilization, as proposed in [36], to prevent instabilities due to the artificial cut of the computational domain.

The mathematical and numerical methods presented above are implemented in the multi-physics high-performance library life^x [37,38] (https://gitlab.com/lifex, https://doi.org/10.5281/zenodo.7852088), developed at MOX, Dipartimento di Matematica, with the collaboration of LaBS, Dipartimento di Chimica, Materiali ed Ingengneria Chimica (both at Politecnico di Milano).

2.4. On the prescription of inlet boundary conditions

The aim of this work is to exploit the mathematical and numerical methods presented in Section 2.3 to provide a reliable description of blood-dynamics in early post-TAVI scenarios. To this aim, a suitable flow rate $\Phi(t)$ should be selected in the inlet boundary condition (1e). Specifically, we impose the physiological waveform taken from [39] (see Fig. 3(b)) and, for each patient, we adapt its magnitude to obtain patient-specific mean flow rate values that match early post-TAVI Doppler TTE cardiac output measurements (see Table 1). Notice that, in absence of any information regarding the patients' Heart Rate (HR), we assumed for all of them the same value HR = 75 bpm.

2.5. Hemodynamic indices

We aim to discriminate between DEG and NODEG patients, thus we perform a post-processing of the numerical results obtained with the model presented in Sections 2.3–2.4. Owing to this analysis, we will be able to find specific criteria able to easily separate the two sub-groups. In this section we describe the tools used for this analysis, whereas in the Results section we will provide the effective thresholds for group separation.

We notice that SVD is a complex phenomenon involving different physical and chemical processes, often occurring at separated space- and time-scales. For such a reason, we believe that the study of individual standard hemodynamic indices, which may describe only one or few of such processes, is not suitable to provide a synthetic information about the separation of the two sub-groups (DEG and NODEG). Therefore, in this work we propose to build new synthetic scores obtained by a combination of standard ones, so that they include multiple hemodynamic features that may influence the degeneration of TAVI valves.

To this aim, in what follows we first describe the standard hemodynamic indices and then how we combine them to obtain the synthetic scores. Specifically, we analyze the following hemodynamic indices:

- Wall Shear Stress:

$$WSS(t, \mathbf{x}) = \|\boldsymbol{\tau} - (\boldsymbol{\tau} \cdot \mathbf{n}) \, \mathbf{n}\|,$$

  where $\mathbf{n}$ represents the unit normal vector to a given surface and $\boldsymbol{\tau} = 2 \left(\mu_{sgs}(\mathbf{u}) + \mu \right) D(\mathbf{u})\mathbf{n}$ is the traction. Additionally, we consider $A^{WSS}(t)$, the area of the aortic wall where WSS is greater than the threshold of 5 Pa. This threshold identifies regions of high WSS, not necessarily pathological. Notice that instantaneous WSS magnitude typically ranges from 1 to 7 [Pa] in straight vessels of the arterial system [40]. High values of WSS can be associated with changes in the endothelial cell behavior, potentially exacerbating inflammation [41];

- Q-criterion:

$$Q(t, \mathbf{x}) = \frac{1}{2} \left(\|W(\mathbf{u})\|^2 - \|D(\mathbf{u})\|^2 \right),$$

  where $W(\mathbf{u}) = \frac{\nabla \mathbf{u} - \nabla^T \mathbf{u}}{2}$ is the vorticity tensor. Positive values of this index identify regions where vorticity dominates over laminar friction. Additionally, we consider $V_Q^\%(t)$, the fraction of volume where Q is greater than a selected threshold [42] of 50 000 Hz^2. This threshold is chosen to properly isolate vortical structures. The proposed volume fraction gives a measure of flow disturbance inside the considered domain. Disturbed flow has a well-proven impact on vascular endothelial cells and contributes to the patho-physiology of clinical conditions such as in-stent re-stenosis as well as aortic valve calcification [43];

- Diastolic Time-Averaged Wall Shear Stress:

$$TAWSS(\mathbf{x}) = \frac{1}{T_D} \int_D WSS \, dt$$

  where D is the diastolic interval and T_D its duration. Additionally, we consider $avgTAWSS$, the average-in-space $TAWSS$ on the aortic face of the bioprosthetic leaflets. Notice that low shear stresses on the aortic side of the aortic valve can enhance the permeability of the endothelial cell barrier with respect to small molecules [44]. In particular, we consider only the diastolic period because the deposition of material on the leaflets mainly occurs during the diastolic phase;

- Oscillatory Shear Index:

$$OSI(\mathbf{x}) = \frac{1}{2} \frac{\| \int_0^T \boldsymbol{\tau} - (\boldsymbol{\tau} \cdot \mathbf{n}) \, \mathbf{n} \, dt \|}{\int_0^T WSS \, dt}.$$

  Additionally, we consider $avgOSI$, the average-in-space OSI on the aortic face of the bioprosthetic leaflets. Oscillatory shear stresses on the aortic side of the valve promote inflammation and calcification [45].

In order to discriminate between DEG and NODEG patients, we assign a score related to each hemodynamic index and we combine them to define SVD-discriminating synthetic scores. In particular, indicating with the bar average values over time, we consider the scalar quantities $\overline{A^{WSS}}, \overline{V_Q^\%}, avgTAWSS, avgOSI$ and, exploiting the inter-patient variability, we normalize their values to make them comparable, as follows.
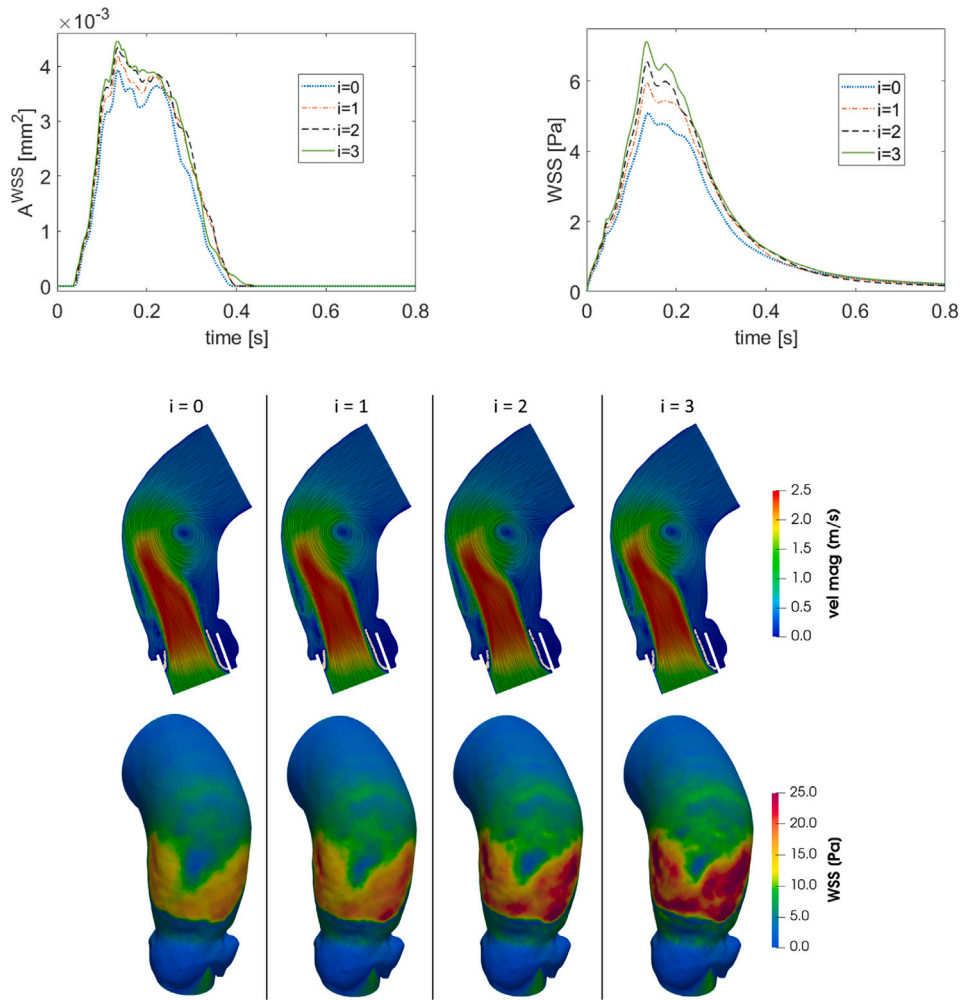
Fig. 4. For different refinement steps i (see Table 2): time evolution of the area of the aortic wall with WSS greater than 5 Pa (top left); time evolution of the average WSS on the lateral boundary of the domain (top right); velocity streamlines, colored by velocity magnitude, on a longitudinal section and WSS on the aortic wall at the systolic-peak (bottom).

We split the study population (14 patients) into a normalization set (12 patients) and a blind set (2 patients: DEG7 and NODEG7), we compute the first (ψ_1) and third (ψ_3) quartiles of each score in the normalization set and we linearly project the interval $[\psi_1 - 1.5 * IQR, \psi_3 + 1.5 * IQR]$ into the interval $[-1, 1]$, where $IQR = \psi_3 - \psi_1$ is the interquartile range. So that, four hemodynamic scores, with the associated "normalized" version, related to the proposed hemodynamic indices are assigned to each patient.

The SVD-discriminating synthetic scores are defined as a linear combination of the mean and maximum values of these four normalized hemodynamic scores. In particular, by splitting the hemodynamic indices related to the aorta and the ones related to the leaflets, we consider:

$$Aorta_{score} = max\left\{ \overline{A^{WSS}}_N, \overline{V^{\%}_Q}_N \right\} \tag{2a}$$

$$leaflets_{score} = max\left\{ -avgTAWSS_N, avgOSI_N \right\}, \tag{2b}$$

where the subscript N identifies the normalized scores and the opposite of $avgTAWSS_N$ is considered in order to associate low values of this hemodynamic score to high values of the synthetic score. Finally, we introduce a global SVD-discriminating score that synthesizes each considered index:

$$SVD_{score} = \frac{1}{2}\left(mean\left\{ \overline{A^{WSS}}_N, \overline{V^{\%}_Q}_N, -avgTAWSS_N, avgOSI_N \right\} \right)$$

$$+ \frac{1}{2}\left(max\left\{ \overline{A^{WSS}}_N, \overline{V^{\%}_Q}_N, -avgTAWSS_N, avgOSI_N \right\} \right). \tag{3a}$$

We stress that, $Aorta_{score}$, $leaflets_{score}$ and SVD_{score} include, in a synthetic way, multiple hemodynamic features that may influence the degeneration of TAVI valves. This is an accordance with our belief that analyzing such features individually could not account for the complexity of the SVD process.

3. Results

If not explicitly stated, all the results presented in this section are obtained by numerically simulating six complete heartbeats, discarding the first one to remove the influence of the null initial condition and averaging quantities between the remaining five.

Simulations were run in parallel on 56 cores of Xeon E5-2640v4@2.4 GHz CPU's, using the computational resources available at MOX, Dipartimento di Matematica, Politecnico di Milano. The average computational time for each simulation (i.e. for six complete heartbeats) is 28.3 ± 4.2 h.

3.1. On the choice of the computational mesh

The mesh size is chosen after a mesh convergence analysis performed for patient NODEG2 during the first heartbeat and based on

Table 2

Mesh convergence analysis: i is the refinement step; h_{max}^i is the maximum mesh size; h_{BL}^i is the boundary layer's finest layer thickness; $\mathcal{R}^i = h_{max}^{i+1}/h_{max}^i = h_{BL}^{i+1}/h_{BL}^i$ is the refinement factor; $d^i = |\overline{A^{WSS}}_i - \overline{A^{WSS}}_{i+1}|/\overline{A^{WSS}}_i$ is the absolute relative difference.

i	h_{max}^i	h_{BL}^i	$\mathcal{R}^i$	d^i
0	2.95 mm	0.23 mm	0.77	12.78%
1	2.27 mm	0.18 mm	0.77	4.35%
2	1.75 mm	0.14 mm	0.77	0.61%
3	1.35 mm	0.11 mm		

Table 3

Comparison between maximum blood velocity magnitude through the aortic valve obtained from Continuous wave Doppler TTE and computed from the CFD simulations as the average ± standard deviation over the selected family of lines.

ID	$V_{max}^{Doppler}$ [m/s]	V_{max}^{CFD} [m/s]	ID	$V_{max}^{Doppler}$ [m/s]	V_{max}^{CFD} [m/s]
DEG1	2.6	2.88 ± 0.03	NODEG1	2.5	2.55 ± 0.02
DEG4	2.6	2.54 ± 0.06	NODEG2	2.0	2.20 ± 0.06
DEG5	2.5	2.63 ± 0.02	NODEG4	2.5	2.54 ± 0.03
DEG6	2.6	2.78 ± 0.03	NODEG5	2.3	2.27 ± 0.04
DEG7	2.4	2.53 ± 0.02	NODEG6	2.1	2.85 ± 0.04

sequential refinements. In particular, since we are interested in comparing the average quantities appearing in the proposed hemodynamic scores (see Section 2.5), we stop the refinement when the mean value in time $\overline{A^{WSS}}$ of the area of the aortic wall with WSS greater than 5 Pa shows a relative difference below 1%, as a consequence of a refinement factor $\mathcal{R} = 0.77$ (that is the ratio of two consecutive mesh sizes is equal to 0.77). We identify two characteristic sizes for our meshes, the maximum mesh size h_{max} and the boundary layer's finest layer thickness h_{BL}. Table 2 shows the results of the convergence analysis: $h_{max} = 1.75$ mm and $h_{BL} = 0.14$ mm are selected using the considered criterion. Moreover, in Fig. 4 (top left) we depict the evolution in time of $A^{WSS}(t)$ which confirms the convergence behavior of our analysis.

For the sake of completeness, in Fig. 4 (top right and bottom) we report, for the different refinement steps, the time evolution of the average WSS on the lateral boundary of the domain, the velocity streamlines on a longitudinal plane and the WSS on the aortic wall at the systolic-peak time instant. Notice that the velocity streamlines are almost equivalent, slight differences can be found close to the vortices, whereas the WSS visualization shows some differences between the refinement steps, also confirmed by the average WSS plot.

Finally, in order to assess the LES model quality we consider the Pope criterion [46], namely we compute the fraction of turbulent kinetic energy in the resolved scales $M(\mathbf{x}, t)$:

$$M(\mathbf{x}, t) = \frac{k_{res}(\mathbf{x}, t)}{k_{res}(\mathbf{x}, t) + k_{sgs}(\mathbf{x}, t)}$$

where $k_{res}(\mathbf{x}, t)$ is the resolved turbulent kinetic energy per unit mass and $k_{sgs}(\mathbf{x}, t) = \mu_{sgs}(\mathbf{x}, t)^2/(C\Delta\rho)^2$ [47] is the sub-grid scale turbulent kinetic energy, with $C = 1.5$ a LES constant [25] and $\Delta = 1$ mm a representative average value of the mesh size. Notice that a good LES model should be able to resolve at least 80% of the total turbulent kinetic energy [46,48]. We analyzed the same patient considered for the mesh convergence and we found that the fraction of volume in the computational domain where $M > 0.8$ is always greater than 88%, with mean value during the heartbeat of 93%. Thus we deem our discretization strategy as sufficiently refined for the considered LES model.

3.2. On the accuracy of the virtual stent implantation

The early post-TAVI computational domains obtained following the procedure presented in Section 2.2 are reported in Fig. 5 together with the positioned bioprosthetic leaflets in open configurations. Notice that we were not able to extract useful insights regarding the discrimination between DEG and NODEG patients from an analysis based only on the anatomical features, such as aortic orifice's area, sinotubular junction's diameter and ascending aorta's curvature.

In addition to the pre-operative CT scans available for each patient in the study population, for patient DEG1 and NODEG1 we also have at disposal post-operative CT scans taken few years after the intervention, which can be used to validate the virtual stent implantation procedure. In particular, starting from these post-operative CT images we reconstruct the post-operative aortic geometry and the implanted stent, and we compare the position of the latter with that obtained by the virtual insertion in the pre-operative scenario. Fig. 6 shows the positions of the

reconstructed (in red) and of the virtually inserted (in green) stents. We observe that the position and orientation of the virtual stent inside the pre-operative geometry is in qualitative good agreement with those of the implanted stent inside the post-operative geometry.

Moreover, the reconstructed implanted stent (in red) shows a circular cross section in the view from the left ventricle, supporting our decision to consider a cylindrical virtual stent.

3.3. Validation of blood velocity numerical results

For a subset of patients in the study population we have at disposal also Continuous wave Doppler TTE data (see Section 2.1), which provides the maximum systolic blood velocity magnitude through the aortic valve. We use this information to assess the accuracy of our CFD results.

In accordance with the clinical measure, we consider a family of lines perpendicular to the valvular plane and going from the ventricular inlet to the ascending aorta, thus covering the entire region of the leaflets. In particular, in order to cope with the uncertainty associated to the Doppler measurement, we analyze five lines inside a cylinder (radius = 3 mm) which passes through the center of the valve. Then, we select the value of the maximum systolic velocity magnitude obtained by our numerical experiments over each line, and finally we compute the mean and standard deviation (V_{max}^{CFD}) of such values. In Table 3 we report, for each patient with available clinical data, the results of our comparison. The table shows that there is a good agreement between the Doppler and CFD results, with eight patients out of ten showing differences lower than or equal to 0.2 m/s. There is a slightly greater discrepancy for patient DEG1 (2.6 vs. 2.88 ± 0.03) and a non-negligible difference for patient NODEG6 (2.1 vs. 2.85 ± 0.04). These results are going to be discussed in Section 4.

3.4. Analysis of the numerical results

In Fig. 5, the blood velocity streamlines resulting from the CFD analysis are depicted on a longitudinal plane at two time instants: one during systole and one during diastole. The CFD results show that, during systole, the presence of the bioprosthetic TAVI valve results in the formation of a high velocity jet inside the ascending aorta together with some vortical structures. The morphology of the jet and of the vortical structures depends on the patient-specific geometries and cardiac outputs (see Table 1). The results at the diastolic time are characterized by chaotic velocity streamlines throughout the computational domain for each patient.

Together with this jet, also vortical structures collide against the aortic wall, giving rise to a highly disturbed flow and great shear stresses on the wall. This is reported for a representative case (patient DEG3) in Fig. 7, where the WSS pattern is shown to follow the evolution of the vortical structures, which are highlighted by the Q-criterion. In the same figure we report also the pressure field at a time instant in early systole on a longitudinal plane. This result shows a relevant pressure drop across the bioprosthetic valve and low pressure zones in the ascending aortic tract, in correspondence of the vortices. Finally, we report also the hemodynamic indices presented in Section 2.5.
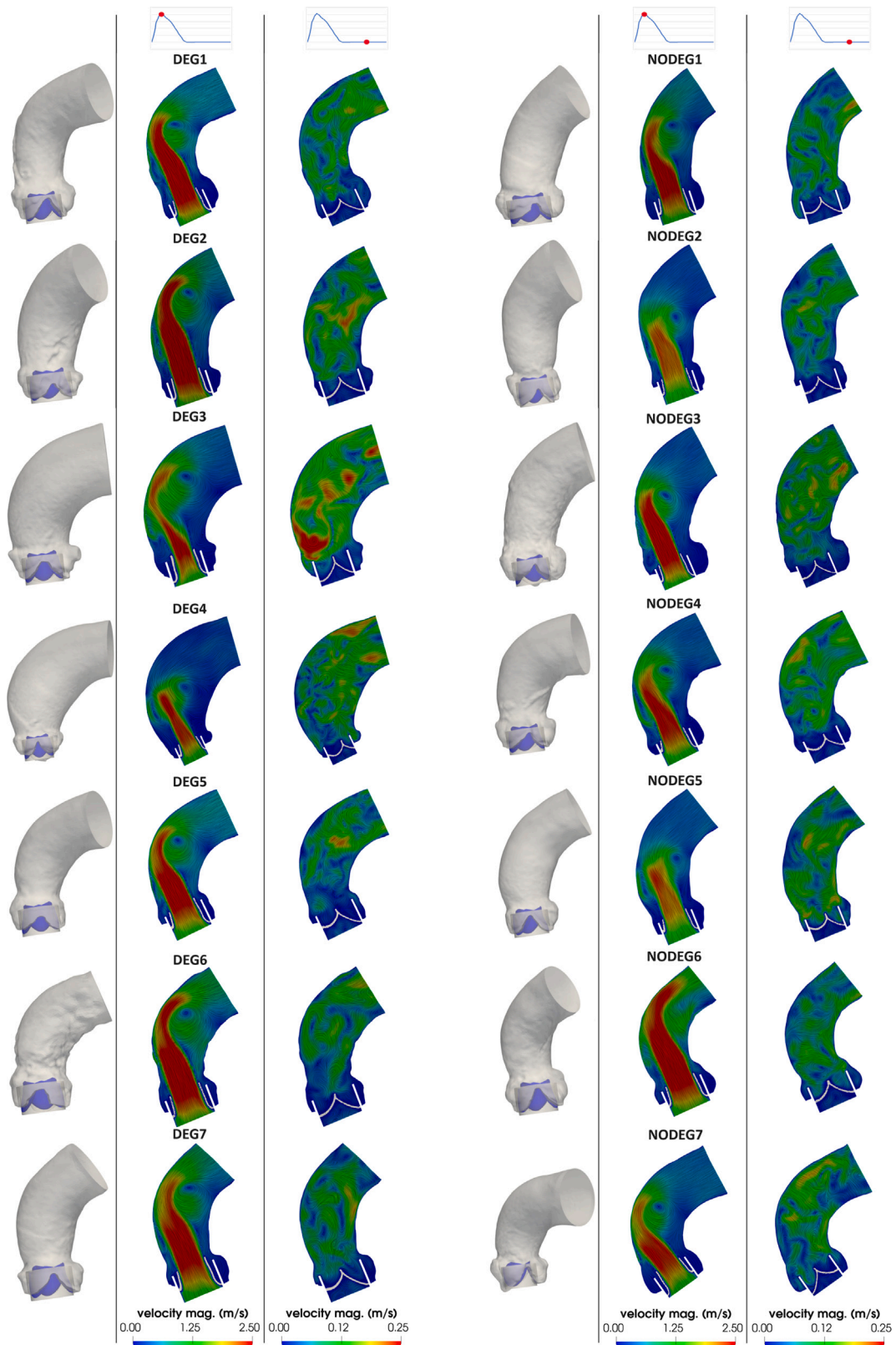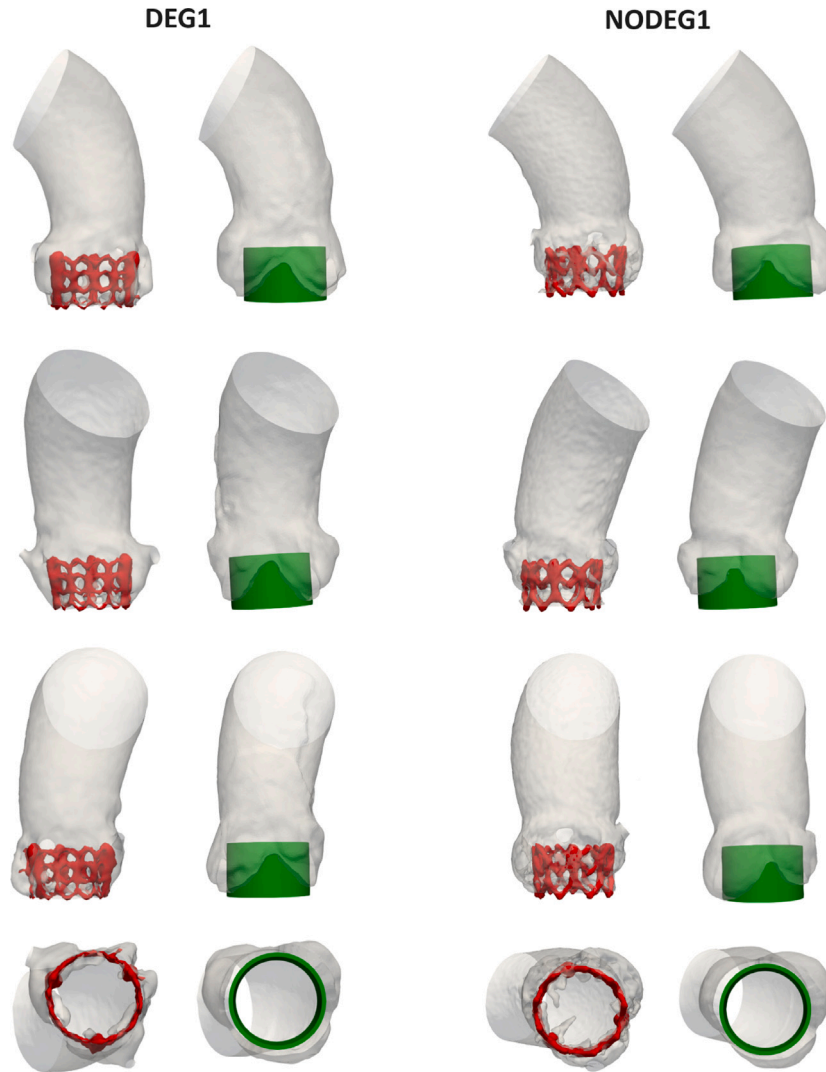
Fig. 5. Computational domain with bioprosthetic leaflets (left); Velocity streamlines on a longitudinal section at the systolic-peak (middle) and a representative diastolic (right) instants.

DEG1

NODEG1

Fig. 6. Validation of virtual stent implantation for patients DEG1 and NODEG1. Three different frontal views and the view from the left ventricle are reported in the different rows. Left: Aortic geometry and implanted stent (in red) reconstructed from the post-operative CT scan; Right: computational domain after virtual stent insertion (in green).

We also notice that, in our CFD analysis, the pressure drop values across the aortic valve are in the range [10–20] mmHg, consistent with standard values for mildly stenotic valves [49], which is the case after TAVI.

3.5. Statistical analysis

In Table 4 we report, for each patient, the hemodynamic scores introduced in Section 2.5. In Fig. 8(a) we report the corresponding boxplots, which highlight that the scores are distributed differently in the DEG and NODEG patients. In particular, each hemodynamic index shows an increased variability (wider boxes) in the DEG patients with respect to the NODEG ones, with the only exception of $avgTAWSS$ which takes low values for each DEG patient.

To assess differences between the two sub-groups of patients in terms of each individual hemodynamic score, the Wilcoxon rank-sum test is employed: we found that $avgOSI$ is the only index showing statistically significant differences ($p = 0.007$) between DEG and NODEG patients, whereas for the other indices we have in any case $p > 0.1$. However, $avgOSI$ alone is not able to clearly separate the two groups of patients. This is the reason why we focused on synthetic scores (see Section 3.6).

Table 4
Hemodynamic scores introduced in Section 2.5.

ID	$\overline{A^{WSS}}$	$\overline{V_Q^\%}$	$avgOSI$	$avgTAWSS$
DEG1	1.48×10^{-3}	2.81×10^{-2}	1.43×10^{-1}	1.03×10^{-2}
DEG2	1.25×10^{-3}	3.68×10^{-2}	1.57×10^{-1}	1.21×10^{-2}
DEG3	1.48×10^{-3}	2.46×10^{-2}	1.61×10^{-1}	1.18×10^{-2}
DEG4	1.41×10^{-3}	1.30×10^{-2}	1.35×10^{-1}	0.98×10^{-2}
DEG5	1.16×10^{-3}	3.20×10^{-2}	1.65×10^{-1}	0.79×10^{-2}
DEG6	1.04×10^{-3}	4.18×10^{-2}	1.51×10^{-1}	0.91×10^{-2}
DEG7	0.96×10^{-3}	3.43×10^{-2}	1.94×10^{-1}	1.24×10^{-2}
NODEG1	1.20×10^{-3}	2.86×10^{-2}	1.43×10^{-1}	2.34×10^{-2}
NODEG2	0.92×10^{-3}	1.69×10^{-2}	1.31×10^{-1}	0.87×10^{-2}
NODEG3	1.30×10^{-3}	1.88×10^{-2}	1.50×10^{-1}	1.01×10^{-2}
NODEG4	1.24×10^{-3}	2.23×10^{-2}	1.33×10^{-1}	0.90×10^{-2}
NODEG5	1.00×10^{-3}	2.13×10^{-2}	1.30×10^{-1}	3.21×10^{-2}
NODEG6	1.29×10^{-3}	4.35×10^{-2}	1.29×10^{-1}	4.03×10^{-2}
NODEG7	1.27×10^{-3}	2.72×10^{-2}	1.41×10^{-1}	1.10×10^{-2}

3.6. Synthetic scores

In Fig. 8(b) we visualize each patient in a two-dimensional space using the synthetic scores $Aorta_{score}$ and $leaflets_{score}$ introduced in
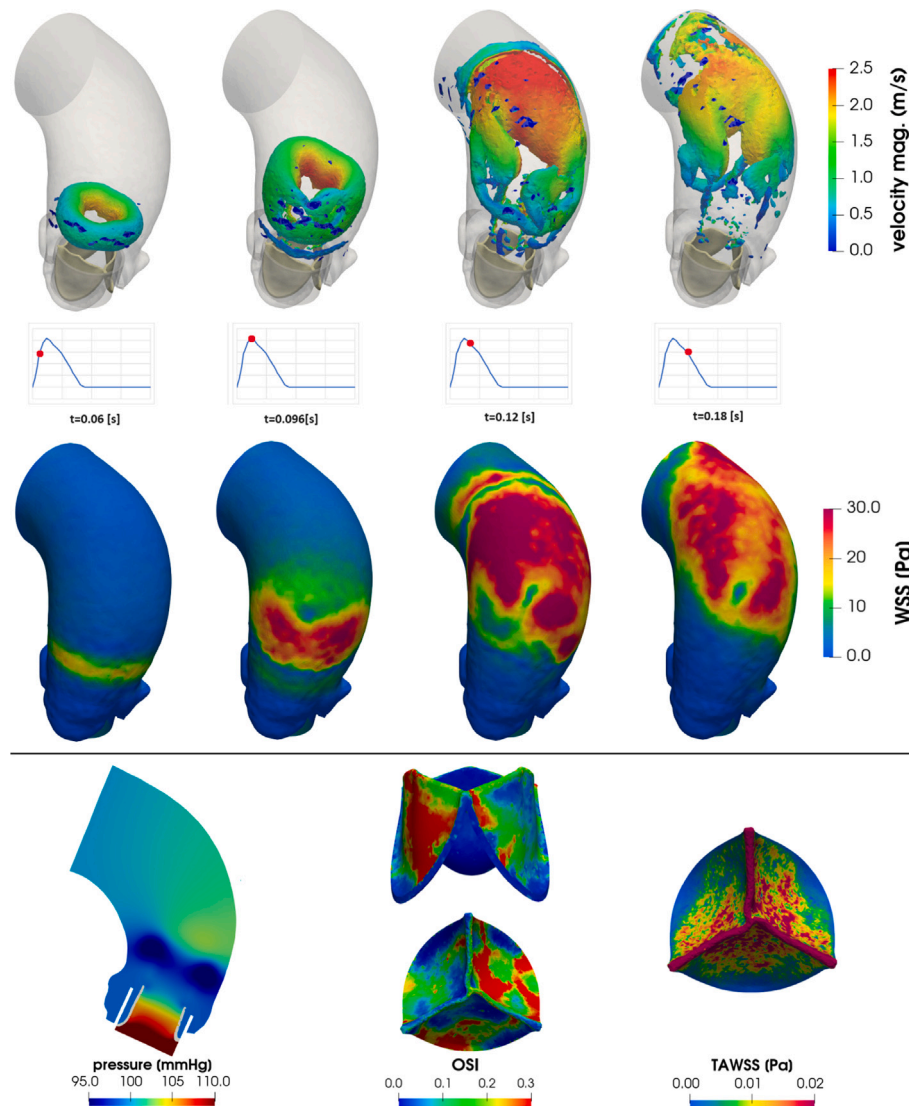
Fig. 7. Post-processing of the numerical results for patient DEG3. Top row: time evolution of vortical structures, isolated exploiting the Q-criterion ($Q > 50\,000$ Hz^2) and colored by velocity magnitude. Middle row: time evolution of WSS on the aortic wall. Bottom row: pressure field at a time instant in early systole (left); OSI on the bioprosthetic leaflets during both systole and diastole (middle); diastolic TAWSS on the bioprosthetic leaflets (right).

Section 2.5. The figure shows that DEG and NODEG patients can be linearly separated in this two-dimensional space. This result highlights that, by considering the synthetic scores instead of the individual ones, we are able to discriminate more efficiently the two groups of patients.

We report in Table 5, for both the normalization and blind sets, the global SVD_{score} introduced in Section 2.5. In particular, for the normalization set DEG patients present SVD_{score} values greater than or equal to 0.15, whereas NODEG patients present a score lower than 0.15. Thus, this global synthetic score seems to be able to discriminate between the two sub-groups of patients and can be interpreted as likelihood of developing a premature onset of SVD. This is confirmed by the application of this score to two cases (DEG7 and NODEG7) not used during the normalization. Specifically, as reported in Table 5 we obtained $SVD_{score} = 0.56$ for DEG7 and $SVD_{score} = 0.09$ for NODEG7.

4. Discussion

Structural Valve Deterioration (SVD) is a complex phenomenon with its underlying mechanisms still not entirely understood. Recent studies suggest the host's immune response is a significant factor in SVD pathogenesis, manifested by a combination of processes phenocopying

Table 5
Global SVD-discriminating score SVD_{score}. Patient DEG7 and NODEG7 belong to the blind set.

ID	SVD_{score}	ID	SVD_{score}
DEG1	0.29	NODEG1	−0.06
DEG2	0.23	NODEG2	0.04
DEG3	0.31	NODEG3	0.11
DEG4	0.15	NODEG4	0.12
DEG5	0.27	NODEG5	−0.34
DEG6	0.30	NODEG6	0.11
DEG7	0.56	NODEG7	0.09

atherosclerosis and calcification of native aortic valves [10]. Furthermore, calcific aortic valve disease is an active process characterized by lipoprotein deposition and chronic inflammation [50]. Consequently, we posit that aortic hemodynamics could have an influence on SVD development.

Given the above considerations, our study introduces novel hemodynamic indices capable of discriminating between patients with or without SVD. To achieve this we construct early post-TAVI computational scenarios which have been validated against Echo Doppler data.
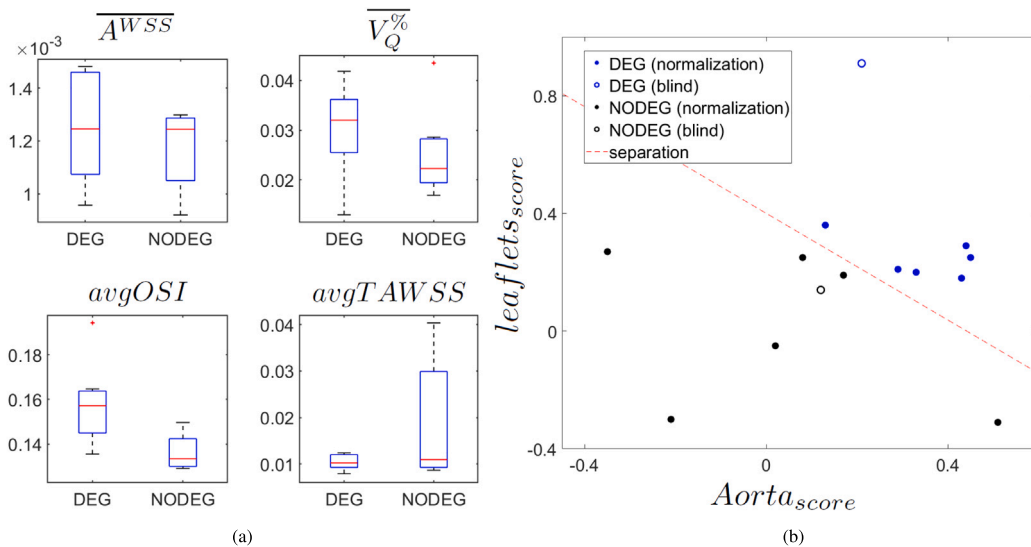
Fig. 8. (a) Visualization of the hemodynamic scores distribution in the DEG and NODEG patients using boxplots. (b) Visualization of DEG and NODEG patients in a two-dimensional space given by $Aorta_{score}$ and $leaflets_{score}$.

Specifically, we investigate blood-dynamics also downstream of the valve because we hypothesize that the mutual hemodynamic effects on both the leaflets and the aortic root may play a major role.

Notice that in this study we exploit only data routinely acquired during the diagnosis and treatment of Aortic Stenosis (AS), such as pre-operative CT scans and post-operative Doppler TTE.

Regarding the inflow boundary conditions, we stress that we are imposing a patient-specific mean flow rate value by using early post-TAVI Doppler TTE cardiac output measurements. In absence of other data, we make the assumption that the physiological waveform taken from literature (see Fig. 3(b)) could be effective for all the cases. This hypothesis is validated by the comparison of blood velocity numerical results with continuous wave Doppler TTE (see Table 3). Only patients DEG1 and NODEG6 show a difference in terms of the comparison greater than 0.2 m/s. This can be due to an oversizing of the implanted valve resulting in a larger effective area with respect to virtually implanted valve. However, we cannot check this, being a retrospective study.

As for the hemodynamic scores (see Section 2.5), we notice that we select them in order to propose a scoring system able to clearly isolate the DEG sub-group of patients. We plan to refine the definition of the scores in future works, possibly further normalizing them using anatomical or functional features.

The results of our study suggest that post-operative hemodynamics should be taken into account for a complete assessment of TAVI bioprosthetic valves long-term durability. Indeed, we identified a hemodynamic score ($avgOSI$) that shows statistically significant differences ($p = 0.007$) between DEG and NODEG patients and we defined purely hemodynamic-based synthetic scores able to discriminate between the two sub-groups of patients. As a consequence, the proposed hemodynamic indices, possibly together with other SVD predictors [3], can assist clinicians in a patient-specific planning of follow-up exams based on the risk of prematurely developing SVD. Specifically, patients who are predicted to encounter a premature onset of SVD could be monitored in a systematic way by the hospital where TAVI is performed in order to avoid the dispersion of the patients, which represents a strong limit of the follow-up procedure.

We remember that our model is subject to three main modeling assumptions which were made in order to reduce the computational effort and to make our analysis potentially reliable for clinical purposes:

- Representing the stent with an *a priori*-decided cylindrical shape without performing a Finite Elements inflation mechanical simulation (the latter was performed for example in [51]). This choice allows us to account for calcification only in terms of the computation of the effective barycenter of the annulus, where the stent is positioned, but not for the possible morphological changes of the stent. However, we believe that our assumption is reasonable since, after the deployment, balloon-expandable valves are expected to achieve an almost cylindrical shape [52], as also proven for DEG1 and NODEG1 by the comparison reported in Fig. 6;

- Neglecting leaflets' dynamics and leaflets' Fluid-Structure Interaction. We model the valve's leaflets in an on/off modality by assuming rigid systolic and diastolic configurations. This prevents us from accounting for the opening and closure mechanisms which may have an impact on the systolic jet and diastolic vortices. Moreover, we could not account for the fluttering of the open leaflets during systole. However, we believe that using a realistic effective opening area for the bioprosthetic valve, as done in this work, is the most influential feature, related to valve modeling, to accurately describe post-TAVI aortic hemodynamics, since this allows us to achieve realistic velocity and stress magnitudes inside the aorta;

- Describing the aortic wall as rigid. We accept this simplification since we are analyzing elderly patients often showing calcification in the ascending aorta, thus we expected a limited elasticity of the vessel wall.

There are other points that should be discussed as possible limitations of the work:

- We neglected the wire-frame design of the stent. This is accurate only on the stent's ventricular side, due to the presence of the inner skirt. This limitation could potentially have an impact on secondary diastolic flows which may cross the wire-frame and thus, in particular, on the leaflets' OSI and TAWSS scores. We plan to provide a wire-frame design for the aortic side of the stent in future studies;

- We included patient-specific information concerning only mean flow rates in the boundary conditions. Prescribing completely patient-specific inlet conditions can be achieved by exploiting 4D-Flow Magnetic Resonance Imaging [53]. This could not be done in the present work due to the retrospective nature of the study.

Alternatively, one could build more realistic 4D velocity profiles using, e.g., the techniques presented in [54];

- We did not consider the interaction between fluid and the prosthesis. This is done according to the results of the preliminary study [11], where no significant indices were identified from this interaction;

- We considered an idealized model (taken from [20]) for the bio-prosthetic leaflets, however with pericardial mechanical properties, similar to Edwards SAPIEN valves. The geometry of the leaflets in open configuration could have an impact on aortic hemodynamics. However, since we are neglecting valve dynamics (on-off modality) and since TAVI should restore a physiological open configuration of the valve, we assume that, for the aim of this CFD analysis, our choice for the leaflets could be reasonable. Indeed, our interest is to have a fully open and fully closed configuration of the leaflets, and the chosen approach allows us to effectively model these two scenarios. In particular, in our CFD analysis, we found values of pressure drop across the valve in the range [10–20] mmHg (see Section 3.4). Whereas, in the Finite Element analysis carried out in [20] to obtain the open configuration, the authors imposed values in the range of 2 mmHg. The fact that our pressure drop is larger guarantees the complete opening of our leaflets;

- We performed only a qualitative validation, based on looking at the reconstructed geometries, of the virtual stent implantation (see Fig. 6). A more quantitative analysis based on the mapping of the post-TAVI aortic geometry onto the pre-TAVI aortic geometry will be required in future studies to strengthen our approach;

- We did not account for coronary flow. Coronary flow is thought to mainly come from the elastic relaxation of the aortic wall following its systolic expansion [55,56], but we cannot describe this process due to the rigid wall assumption in the proposed CFD setting (see Section 2.3);

- We analyzed only fourteen patients. We understand that this number is probably too small to provide significant answers in terms of the influence of hemodynamics on SVD; however, collecting a greater number of data related to degenerated cases with available follow-up is difficult due to both the relative young age of the TAVI procedure and the high dispersion of patients after the implant;

- We used the same heart rate for all the patients due to the absence of such data for our cases. This may have an influence on fluid dynamics patterns and thus on the proposed hemodynamic scores. This deserves further and deeper investigations.

CRediT authorship contribution statement

Luca Crugnola: Writing – review & editing, Writing – original draft, Visualization, Validation, Software, Methodology, Investigation, Formal analysis, Data curation, Conceptualization. **Christian Vergara:** Writing – review & editing, Writing – original draft, Visualization, Supervision, Project administration, Methodology, Funding acquisition, Conceptualization. **Laura Fusini:** Writing – review & editing, Validation, Resources, Data curation, Conceptualization. **Ivan Fumagalli:** Writing – review & editing, Software, Methodology, Conceptualization. **Giulia Luraghi:** Writing – review & editing, Resources, Data curation, Conceptualization. **Alberto Redaelli:** Writing – review & editing, Methodology. **Gianluca Pontone:** Writing – review & editing, Supervision, Funding acquisition, Conceptualization.

Ethics approval

The study was approved from the Institutional Review Board of Centro Cardiologico Monzino and registered with number R1264/20. Informed consent was obtained from all patients.

Declaration of competing interest

The authors declare that they have no known competing financial interests or personal relationships that could have appeared to influence the work reported in this article.

References

[1] T.J. Cahill, M. Chen, K. Hayashida, A. Latib, T. Modine, N. Piazza, S. Redwood, L. Søndergaard, B.D. Prendergast, Transcatheter aortic valve implantation: current status and future perspectives, Eur. Heart J. (ISSN: 0195-668X) 39 (28) (2018) 2625–2634.

[2] A. Vahanian, F. Beyersdorf, F. Praz, M. Milojevic, S. Baldus, J. Bauersachs, D. Capodanno, L. Conradi, M. De Bonis, R. De Paulis, V. Delgado, N. Freemantle, M. Gilard, K.H. Haugaa, A. Jeppsson, P. Jüni, L. Pierard, B.D. Prendergast, J.R. Sádaba, C. Tribouilloy, W. Wojakowski, E.S.D. Group, E.N.C. Societies, 2021 ESC/EACTS Guidelines for the management of valvular heart disease: Developed by the Task Force for the management of valvular heart disease of the European Society of Cardiology (ESC) and the European Association for Cardio-Thoracic Surgery (EACTS), Eur. Heart J. (ISSN: 0195-668X) 43 (7) (2021) 561–632.

[3] M. Guglielmo, L. Fusini, M. Muratori, G. Tamborini, V. Mantegazza, D. Andreini, A. Annoni, M. Babbaro, A. Baggiano, E. Conte, et al., Computed tomography predictors of structural valve degeneration in patients undergoing transcatheter aortic valve implantation with balloon-expandable prostheses, Eur. Radiol. (2022) 1–11.

[4] M.J. Mack, M.B. Leon, V.H. Thourani, R. Makkar, S.K. Kodali, M. Russo, S.R. Kapadia, S.C. Malaisrie, D.J. Cohen, P. Pibarot, et al., Transcatheter aortic-valve replacement with a balloon-expandable valve in low-risk patients, N. Engl. J. Med. 380 (18) (2019) 1695–1705.

[5] J.J. Popma, G.M. Deeb, S.J. Yakubov, M. Mumtaz, H. Gada, D. O'Hair, T. Bajwa, J.C. Heiser, W. Merhi, N.S. Kleiman, J. Askew, P. Sorajja, J. Rovin, S.J. Chetcuti, D.H. Adams, P.S. Teirstein, G.L. Zorn, J.K. Forrest, D. Tchétché, J. Resar, A. Walton, N. Piazza, B. Ramlawi, N. Robinson, G. Petrossian, T.G. Gleason, J.K. Oh, M.J. Boulware, H. Qiao, A.S. Mugglin, M.J. Reardon, Transcatheter aortic-valve replacement with a self-expanding valve in low-risk patients, N. Engl. J. Med. 380 (18) (2019) 1706–1715.

[6] S. Mirsadraee, S. Sellers, A. Duncan, A. Hamadanchi, D. Gorog, Bioprosthetic valve thrombosis and degeneration following transcatheter aortic valve implantation (TAVI), Clin. Radiol. 76 (1) (2021) 73–e39.

[7] G. Costa, E. Criscione, D. Todaro, C. Tamburino, M. Barbanti, Long-term transcatheter aortic valve durability, Interv. Cardiol. Rev. 14 (2) (2019) 62.

[8] M. Muratori, L. Fusini, G. Tamborini, P. Gripari, S. Ghulam Ali, M. Mapelli, F. Fabbiocchi, P. Trabattoni, M. Roberto, M. Agrifoglio, et al., Five-year echocardiographic follow-up after TAVI: structural and functional changes of a balloon-expandable prosthetic aortic valve, Eur. Heart J.-Cardiovasc. Imaging 19 (4) (2018) 389–397.

[9] N. Côté, P. Pibarot, M.-A. Clavel, Incidence, risk factors, clinical impact, and management of bioprosthesis structural valve degeneration, Curr. Opin. Cardiol. 32 (2) (2017) 123–129.

[10] A.E. Kostyunin, A.E. Yuzhalin, M.A. Rezvova, E.A. Ovcharenko, T.V. Glushkova, A.G. Kutikhin, Degeneration of bioprosthetic heart valves: update 2020, J. Am. Heart Assoc. 9 (19) (2020) e018506.

[11] I. Fumagalli, R. Polidori, F. Renzi, L. Fusini, A. Quarteroni, G. Pontone, C. Vergara, Fluid-structure interaction analysis of transcatheter aortic valve implantation, Int. J. Numer. Methods Biomed. Eng. 39 (6) (2023) e3704.

[12] G.M. Bosi, C. Capelli, M.H. Cheang, N. Delahunty, M. Mullen, A.M. Taylor, S. Schievano, A validated computational framework to predict outcomes in TAVI, Sci. Rep. 10 (1) (2020) 1–11.

[13] D. Carbonaro, D. Gallo, U. Morbiducci, A. Audenino, C. Chiastra, In silico biomechanical design of the metal frame of transcatheter aortic valves: multi-objective shape and cross-sectional size optimization, Struct. Multidiscip. Optim. (ISSN: 1615-1488) 64 (4) (2021) 1825–1842.

[14] S. Barati, N. Fatouraee, M. Nabaei, L. Petrini, F. Migliavacca, G. Luraghi, J.F.R. Matas, Patient-specific multi-scale design optimization of transcatheter aortic valve stents, Comput. Methods Programs Biomed. (ISSN: 0169-2607) 221 (2022) 106912.

[15] G. Luraghi, F. Migliavacca, A. García-González, C. Chiastra, A. Rossi, D. Cao, G. Stefanini, J.F.R. Matas, On the modeling of patient-specific transcatheter aortic valve replacement: a fluid–structure interaction approach, Cardiovasc. Eng. Technol. 10 (3) (2019) 437–455.

[16] M. Conti, S. Vandenberghe, S. Marconi, E. Ferrari, R.M. Romarowski, S. Morganti, F. Auricchio, S. Demertzis, Reversed auxiliary flow to reduce embolism risk during TAVI: A computational simulation and experimental study, Cardiovasc. Eng. Technol. 10 (1) (2019) 124–135.

[17] M. Bianchi, G. Marom, R.P. Ghosh, O.M. Rotman, P. Parikh, L. Gruberg, D. Bluestein, Patient-specific simulation of transcatheter aortic valve replacement: impact of deployment options on paravalvular leakage, Biomech. Model. Mechanobiol. 18 (2) (2019) 435–451.

[18] D. Dvir, T. Bourguignon, C.M. Otto, R.T. Hahn, R. Rosenhek, J.G. Webb, H. Treede, M.E. Sarano, T. Feldman, H.C. Wijeysundera, et al., Standardized definition of structural valve degeneration for surgical and transcatheter bioprosthetic aortic valves, Circulation 137 (4) (2018) 388–399.

[19] D. Todaro, A. Picci, M. Barbanti, Current TAVR devices, Card Interv. Today 11 (2017) 53–58.

[20] G. Luraghi, F. Migliavacca, J.F. Rodriguez Matas, Study on the accuracy of structural and FSI heart valves simulations, Cardiovasc. Eng. Technol. 9 (4) (2018) 723–738.

[21] L. Antiga, M. Piccinelli, L. Botti, B. Ene-Iordache, A. Remuzzi, D.A. Steinman, An image-based modeling framework for patient-specific computational hemodynamics, Med. Biol. Eng. Comput. 46 (11) (2008) 1097–1112.

[22] S. Jung, F. Ammon, S. Smolka, M. Moshage, M. Marwan, S. Achenbach, Commissural misalignment independently predicts leaflet thrombosis after transcatheter aortic valve implantation, Clin. Res. Cardiol. (2023).

[23] A. Quarteroni, A. Manzoni, C. Vergara, The cardiovascular system: mathematical modelling, numerical algorithms and clinical applications, Acta Numer. 26 (2017) 365–590.

[24] P.D. Stein, H.N. Sabbah, Turbulent blood flow in the ascending aorta of humans with normal and diseased aortic valves, Circ. Res. 39 (1) (1976) 58–65.

[25] F. Nicoud, H.B. Toda, O. Cabrit, S. Bose, J. Lee, Using singular values to build a subgrid-scale model for large eddy simulations, Phys. Fluids 23 (8) (2011) 085106.

[26] M. Rieth, F. Proch, O. Stein, M. Pettit, A. Kempf, Comparison of the Sigma and Smagorinsky LES models for grid generated turbulence and a channel flow, Comput. & Fluids (ISSN: 0045-7930) 99 (2014) 172–181.

[27] L. Bennati, V. Giambruno, F. Renzi, V. Di Nicola, C. Maffeis, G. Puppini, G.B. Luciani, C. Vergara, Turbulent blood dynamics in the left heart in the presence of mitral regurgitation: a computational study based on multi-series cine-MRI, Biomech. Model. Mechanobiol. 22 (6) (2023) 1829–1846.

[28] R.M. Lancellotti, C. Vergara, L. Valdettaro, S. Bose, A. Quarteroni, Large eddy simulations for blood dynamics in realistic stenotic carotids, Int. J. Numer. Methods Biomed. Eng. 33 (11) (2017) e2868.

[29] M. Fedele, E. Faggiano, L. Dedè, A. Quarteroni, A patient-specific aortic valve model based on moving resistive immersed implicit surfaces, Biomech. Model. Mechanobiol. 16 (5) (2017) 1779–1803.

[30] I. Fumagalli, M. Fedele, C. Vergara, S. Ippolito, F. Nicolò, C. Antona, R. Scrofani, A. Quarteroni, et al., An image-based computational hemodynamics study of the Systolic Anterior Motion of the mitral valve, Comput. Biol. Med. 123 (2020) 103922.

[31] Y. Xuan, D. Dvir, Z. Wang, J. Ye, J.M. Guccione, L. Ge, E.E. Tseng, Stent and leaflet stresses across generations of balloon-expandable transcatheter aortic valves, Interact. CardioVasc. Thorac. Surg. 30 (6) (2020) 879–886.

[32] L. Formaggia, J.-F. Gerbeau, F. Nobile, A. Quarteroni, Numerical treatment of defective boundary conditions for the Navier–Stokes equations, SIAM J. Numer. Anal. 40 (1) (2002) 376–401.

[33] A. Veneziani, C. Vergara, Flow rate defective boundary conditions in haemodynamics simulations, Internat. J. Numer. Methods Fluids 47 (8–9) (2005) 803–816.

[34] T.E. Tezduyar, Stabilized finite element formulations for incompressible flow computations, Adv. Appl. Mech. 28 (1991) 1–44.

[35] F. Nobile, M. Pozzoli, C. Vergara, Inexact accurate partitioned algorithms for fluid-structure interaction problems with finite elasticity in haemodynamics, J. Comput. Phys. 273 (2014) 598–617.

[36] M.E. Moghadam, Y. Bazilevs, T.-Y. Hsia, I.E. Vignon-Clementel, A.L. Marsden, A comparison of outlet boundary treatments for prevention of backflow divergence with relevance to blood flow simulations, Comput. Mech. 48 (3) (2011) 277–291.

[37] P.C. Africa, Lifex: A flexible, high performance library for the numerical solution of complex finite element problems, SoftwareX (ISSN: 2352-7110) 20 (2022) 101252.

[38] P.C. Africa, I. Fumagalli, M. Bucelli, A. Zingaro, M. Fedele, A. Quarteroni, et al., Lifex-cfd: An open-source computational fluid dynamics solver for cardiovascular applications, Comput. Phys. Comm. 296 (2024) 109039.

[39] K. Capellini, E. Vignali, E. Costa, E. Gasparotti, M.E. Biancolini, L. Landini, V. Positano, S. Celi, Computational fluid dynamic study for aTAA hemodynamics: an integrated image-based and radial basis functions mesh morphing approach, J. Biomech. Eng. 140 (11) (2018).

[40] J.M. Dolan, J. Kolega, H. Meng, High wall shear stress and spatial gradients in vascular pathology: a review, Ann. Biomed. Eng. 41 (7) (2013) 1411–1427.

[41] P. Eshtehardi, A.J. Brown, A. Bhargava, C. Costopoulos, O.Y. Hung, M.T. Corban, H. Hosseini, B.D. Gogas, D.P. Giddens, H. Samady, High wall shear stress and high-risk plaque: an emerging concept, Int. J. Cardiovasc. Imaging 33 (7) (2017) 1089–1099.

[42] C. Vergara, D. Le Van, M. Quadrio, L. Formaggia, M. Domanin, Large eddy simulations of blood dynamics in abdominal aortic aneurysms, Med. Eng. Phys. 47 (2017) 38–46.

[43] J.-J. Chiu, S. Chien, Effects of disturbed flow on vascular endothelium: pathophysiological basis and clinical perspectives, Physiol. Rev. 91 (1) (2011) 327–387.

[44] L. Shu, Z. Yuan, F. Li, Z. Cai, Oxidative stress and valvular endothelial cells in aortic valve calcification, Biomed. Pharmacother. 163 (2023) 114775.

[45] S. Rathan, C.J. Ankeny, S. Arjunon, Z. Ferdous, S. Kumar, J. Fernandez Esmerats, J.M. Heath, R.M. Nerem, A.P. Yoganathan, H. Jo, Identification of side-and shear-dependent microRNAs regulating porcine aortic valve pathogenesis, Sci. Rep. 6 (1) (2016) 25397.

[46] S.B. Pope, Ten questions concerning the large-eddy simulation of turbulent flows, New J. Phys. 6 (1) (2004) 35.

[47] P. Sagaut, Y.-T. Lee, Large eddy simulation for incompressible flows: An introduction. scientific computation series, Appl. Mech. Rev. 55 (6) (2002) B115–B116.

[48] C. Chnafa, S. Mendez, F. Nicoud, Image-based large-eddy simulation in a realistic left heart, Comput. & Fluids 94 (2014) 173–187.

[49] A. Task, P. Elliott, C. Uk, A. Anastasakis, M. Germany, M. Germany, F. Cecchi, P. France, A. Alain, H. France, et al., ESC guidelines on diagnosis and management of hypertrophic cardiomyopathy, Eur. Heart J. 35 (39) (2014) 2733–2779.

[50] D.A. Lerman, S. Prasad, N. Alotti, Calcific aortic valve disease: molecular mechanisms and therapeutic approaches, Eur. Cardiol. Rev. 10 (2) (2015) 108.

[51] S. Pasta, C. Gandolfo, Computational analysis of self-expanding and balloon-expandable transcatheter heart valves, Biomechanics 1 (1) (2021) 43–52.

[52] J. Li, W. Yan, W. Wang, S. Wang, L. Wei, Comparison of balloon-expandable valve and self-expandable valve in transcatheter aortic valve replacement: A patient-specific numerical study, J. Biomech. Eng. 144 (10) (2022) 104501.

[53] F. Sturla, F. Piatti, M. Jaworek, F. Lucherini, F.R. Pluchinotta, S.V. Siryk, D. Giese, R. Vismara, G. Tasca, L. Menicanti, et al., 4D flow MRI hemodynamic benchmarking of surgical bioprosthetic valves, Magn. Reson. Imaging 68 (2020) 18–29.

[54] S. Saitta, L. Maga, C. Armour, E. Votta, D.P. O'Regan, M.Y. Salmasi, T. Athanasiou, J.W. Weinsaft, X.Y. Xu, S. Pirola, et al., Data-driven generation of 4D velocity profiles in the aneurysmal ascending aorta, Comput. Methods Programs Biomed. 233 (2023) 107468.

[55] F.L. Abel, Influence of aortic compliance on coronary blood flow, Circ. Shock 12 (4) (1984) 265–276.

[56] M.C. Leung, I.T. Meredith, J.D. Cameron, Aortic stiffness affects the coronary blood flow response to percutaneous coronary intervention, Am. J. Physiol.-Heart Circ. Physiol. 290 (2) (2006) H624–H630.